QuikSCAT normalized radar cross section noise characterization for coastal wind field retrieval

OSI_VS20_03

Authors: **G. Grieco**[1], M. Portabella[2], J. Vogelzang[3], A. Verhoef[3], A. Stoffelen[3]

[1] Institute of Marine Sciences (ISMAR-CNR)

[2] Barcelona Expert Center (BEC ICM-CSIC)

[3] Koninklijk Nederlands Meteorologisch Instituut (KNMI)

Visiting Scientist Activity

Technical Report Date:

30 September 2021

Contents

Abstract

An assessment of the noise affecting the QuikSCAT Normalized Radar Cross Sections (σ_0s) is carried out in this study. The estimation of K_p ($\hat{K}_p$) is compared to the median of the K_p values ($\tilde{K}_p$) provided in the Level 1B Full Resolution (L1B) file with orbit number 40651, dated 10^{th} of April 2007, and the main differences are discussed. A sensitivity analysis aiming at assessing the presence of any dependencies with respect to (w.r.t.) different wind regimes, the kind of scattering surface, the scatterometer view and the polarization of the signal is carried out. In addition, the presence of any biases is assessed and discussed. Finally, a theoretical σ_0 distribution model is proposed and validated against the true measurements.
The main outcomes of this study demonstrate that H-Pol measurements are noisier than those V-Pol and that the noise lowers with increasing σ_0 levels,

in line with the expectations. Furthermore, $\hat{K}_p$ may largely differ from $\tilde{K}_p$, especially for the peripheral slices w.r.t. to the footprint (egg) centroid. In particular, the K_p values provided for the slices with indices 0 and 1 seem to be overestimated, while the opposite happens for those with indices 6 and 7. In addition, the $\hat{K}_p$ values estimated over the sea surface are lower than those estimated without making any distinctions among the scattering surfaces. This trend is not seen for $\tilde{K}_p$, for which the differences are almost absent. In addition, $\hat{K}_p$s relating to aft acquisitions do not differ from those relating to fore ones. Furthermore, some inter slice biases up to 0.8 dB are present for H-Pol acquisitions while they are up to 0.3 dB for V-Pol ones, in both cases increasing with the relative distance between the slices, in line with the general Geophysical Model Function (GMF) sensitivity as a function of incidence angle. These biases have a non flat trend w.r.t. the acquisition azimuth angle for both polarizations. These small variations may be due to the changes in wind speed and direction sample for each bin.
The theoretical σ_0 model proves to be effective. It can be used both for simulation studies and for checking the accuracy of the σ_0 noise.

1 Introduction

Most of the human world population lives along the coast. Therefore, their lives are heavily affected by the meteorological phenomena that characterize these areas. In that sense, coastal winds play a relevant role. Indeed, for example, the presence of sea breezes, katabatic winds and orographic winds in general, can strongly characterize local micro climates and, for example, wind energy potential. Furthermore, they play a fundamental role in the determination of local sea currents and in the dispersion of air pollutants. For all these reasons and for many others that are not mentioned here, the knowledge of accurate and highly sampled coastal winds is of paramount importance to modern societies.

Scatterometer derived winds represent the golden standard for low to medium spatial resolution applications, with accuracies better than 1 ms^{-1} [1]. However, near the coast, the scatterometer footprints may be contaminated by the presence of land. This can significantly alter the Normalized Radar Cross Section (σ_0) and, therefore, impact the wind retrieval and the coastal sampling. Recently, many efforts have been devoted to optimally process the scatterometer acquisitions near the shore line with the aim of improving both the sampling and the accuracy of the retrieved winds.

The authors of [2] show how to deal with the land contaminated QuikSCAT σ_0 measurements. A similar approach is applied by the authors of [3] to ASCAT. In [4], the authors show a methodology aiming at getting rid of the land contribution from the ASCAT contaminated σ_0 measurements.

In [5], the authors report on the first steps of the European Agency for the Exploitation of Meteorological Satellites (EUMETSAT) Ocean Sea Ice Satellite Application Facilities (OSI-SAF) towards the implementation of a QuikSCAT processor and the consequent creation of a QuikSCAT-derived coastal wind climatology. In [5], the authors show how to model the Spatial Response Function (SRF) of QuikSCAT and compute the Land Contribution Ratio (LCR). In this study, the authors show the differences between the SRFs obtained by implementing the analytical model described in [6] and those retrieved from a pre-computed Look-up table (LUT) of SRFs parameterized by means of the slice centroid latitude, the orbit time and the acquisition azimuth angle. In particular, they show how these differences may impact the LCR in a non-negligible way. In addition, one of the main conclusions of that study is that QuikSCAT σ_0s are excessively noisy close to the coast, and that a proper noise characterization is needed before implementing any wind retrieval processors. An accurate noise characterization is important in the inverse problem [7]. In this study we present a methodology to assess the QuikSCAT σ_0 noise, namely K_p and its accuracy. A sensitivity

analysis is shown, aiming at detecting the presence of any inter slice biases and of any biases trends w.r.t. the acquisition azimuth angle. The estimated K_p ($\hat{K}_p$) is then compared to the median of the K_p values ($\tilde{K}_p$) provided in the L1B files [8] [9]. In section 2 a brief background on the definition of K_p and how it can be modeled according to some instrumental parameters ([10]) is presented. The theoretical σ_0 distribution derived from [10] is also shown. Section 3 describes the L1B content relevant to this study. Section 4 describes the methodology that has been used to assess $\hat{K}_p$. Section 5 reports on the results, while their discussion is presented in section 6. Finally a proposal for future work is reported in section 7.

2 Background

K_p is a normalized parameter giving the standard deviation of the measured σ_0 ($\hat{\sigma}_0$) as proportion to the true value of σ_0 (eq. 7 in [10]). It comes out that K_p can be used as a measure of the noise affecting $\hat{\sigma}_0$. Equation 7 of [10] can also be used as an operative definition of K_p. This is to say that given a set of measurements $\hat{\sigma}_{0i}$ ($\forall i \in 1, \ldots, N$), one first computes the standard deviation and the expected value of such set of measurements and then K_p, as the ratio between them. This is what has been done in this study. More details will be given in section 4.
According to [10], K_p can be estimated by means of some instrumental parameters, namely the signal (S) to noise (N) ratio (SNR), the intermediate frequency bandwidth (B_{IF}), the integration time for $S+N$ (τ_{S+N}), the integration time for N (τ_N), the Doppler band spread (B_D) and the Doppler frequency offset (Δf). This parameterization leads to the well known formula:

$$K_p = \sqrt{K_p^{\alpha} + \frac{K_p^{\beta}}{SNR} + \frac{K_p^{\gamma}}{SNR^2}} \tag{2.1}$$

Once one knows the three coefficients K_p^{α}, K_p^{β}, K_p^{γ} and SNR, you can estimate K_p for each available measurement.
K_p^{α}, K_p^{β}, K_p^{γ} and SNR are provided in the L1B files and have been used to compute K_p in this study, according to equation 4.2.
According to [10], both the received signal ($s(t)$) and the noise ($n(t)$) are narrow-band Gaussian stationary processes. It comes out that both the received power of the signal (P_r) and that of the noise (P_n) have a χ^2 distribution. The distribution of their sum (z) can then be modeled as follows:

$$z_{s+n}(t) \sim \frac{\mu_z}{k}\chi_1^2 \tag{2.2}$$

where the expected value of z is $\mu_z = P_r + P_n$ and its variance is $\sigma_z^2 = 2(P_r + P_n)^2$. Following the block diagram depicted in figure 2 of [10], the measured P_r ($\hat{P}_r$) is the output of an integration procedure, performed with the aim of reducing the noise. Therefore, the distribution of $\hat{P}_r$ reads as follows:

$$\hat{P}_r \sim \frac{\mu_{\hat{P}_r}}{k}\chi_k^2 \tag{2.3}$$

where k is the number of degrees of freedom. It can be demonstrated that $k = \frac{2}{K_p^2}$. If one assumes that $\hat{P}_r$ is proportional to $\hat{\sigma}_0$, then the distribution

of $\hat{\sigma}_0$ is identical to that of $\hat{P}_r$ but for the expected value. It is reported here for the sake of completeness:

$$\hat{\sigma}_0 \sim \frac{\mu_{\hat{\sigma}_0}}{k}\chi^2_k \tag{2.4}$$

It appears that if one knows K_p and the expected value of $\hat{\sigma}_0$, one can model the distribution of $\hat{\sigma}_0$. This model can be used for both simulation studies and for validating K_p, by comparing the expected distribution of $\hat{\sigma}_0$ with the true one. An example of such application is presented in section 5.

3 Dataset

The QuikSCAT information thas has been used in this study comes from the L1B files. They can be freely downloaded from the PODAAC web site [8]. Hereafter, some file information content relevant to this report is given. For all the rest, the reader can refer to the official QuikSCAT user's data manual [9]. These files contain the calibrated $\hat{\sigma}_0$s in a time-ordered fashion. $\hat{\sigma}_0$s are organized in 3 dimensional (3D) arrays, whose indices are the telemetry frame (*frame*), the pulse (*pulse*) and the slice (*slice*). The total number of frames is variable from file to file, while the sizes of *pulse* and *slice* are constant, respectively 100 and 8. All the acquisitions are provided with some flags. Three quality control flags are relevant to this study, namely "frame error status" (*frame_err_status*), "frame quality flag" (*frame_qual_flag*) and "σ_0 quality flag" (*sigma0_qual_flag*). According to [9], *frame_err_status* must always be 0, otherwise unusual instrument conditions apply, or bad ephemeris or bad attitude. *frame_qual_flag* brings information about the telemetry quality. [9] recommends that frames with bit 4 equal to 1 (bad data found in frame) not be used. In this study, both requirements are applied.
sigma0_qual_flag accounts for several aspects, each of which is ruled by the 10 of 16 bits described here after. In this study, bits 4 to 9 included (on a 0-based numbering) are required to be 0. This is to say that

- the scatterometer pulse quality is acceptable (bit 4);
- the σ_0 cell algorithm converges (bit 5);
- the frequency shift is within the range of the X factor table (bit 6);
- the spacecraft temperature is within calibration coefficient range (bit 7);
- an applicable attitude record was found for this σ_0 (bit 8);
- interpolated ephemeris data are acceptable for this σ_0 (bit 9)

Bits 0 to 3 account respectively for:

- σ_0 measurement is usable (bit 0);
- SNR value is acceptable (bit 1);
- $\sigma_0 \geq 0$ (bit 2);
- σ_0 is in acceptable range (bit 3);

Bits 10 to 15 are spare, therefore always clear (set to 0). In this study, no requirement is applied to bits 0 to 3 because its final aim is the assessment of K_p, despite the a-posteriori information provided in these flags. Therefore, only general quality control flags are applied. In addition to this flag, the FR files provide also the *slice_qual_flag*. It consists of a 32-bit flag, 4 per each of the 8 slices composing the QuickSCAT "egg". When the four bits are set to 0 they account for the following aspects:

- Gain exceeds peak gain threshold (bit 0);
- $\sigma_0 > 0$ (bit 1);
- SNR level is acceptable (bit 2);
- slice center located (bit 3);

slice_qual_flag is not taken into account in this study for the same reasons explained before.
In addition to the quality flags, FR files provide also the necessary information for computing K_p, namely the coefficients K_p^α, K_p^β, K_p^γ and SNR.
The L1B file naming has the following convention: QS_S1BXXXXX.YYYYJJJHHMM.gz, where XXXXX is the 5 digit orbit number, YYYY is the year, JJJ is the Julian day, HH is the hour and MM is the minute of acquisition. Therefore, each file is uniquely determined by the orbit number. For this reason, hereafter, each reference to the L1B files will happen by means of the orbit number only. Even if the file extension is .gz actually they are in hdf4 format. Most of the results discussed in this study refer to the file with orbit number 40651. However, the consistency of the results has been checked with the files 40652 and 40653. The results of this check are not shown in order to avoid redundancy. For what concerns the trend of the biases w.r.t. the acquisition azimuth angle the results refer to all the files acquired during the 10^{th} of April 2007, namely numbers 40651 to 40664. This has been necessary in order to increase the number of samples. The table depicted in figure 1 gives an idea of the impact of QC on the QuikSCAT measurements of the file 40651. They are divided into H-Pol acquisitions (HH) and V-Pol ones (VV). The impact of each QC flag is shown as a percentage. The total number of acquisitions is 8,992,000, 4,493,232 of which are H-Pol and the remaining 4,498,768 are V-Pol. It is apparent that the general quality flags have a rather low impact, with percentages lower than 1. On the other side, the specific quality flags are more impacting, especially for what concerns the H-Pol acquisitions. It is important to note that the values reported in the row "All" are not the algebraic sum of the previous rows because some occurrences may happen

	% QC HH	% QC VV
sigma0_qual_flag	0.59	0.71
frame_quality_flag	0.00	0.00
frame_err_status	0.01	0.01
All General	0.60	0.72
Peak Gain	9.25	1.56
Negative s0	4.52	2.52
Low SNR	0.88	0.85
Center Loc	0.00	0.00
All	12.70	3.45

Figure 1: Impact of QC on the QuikSCAT measurements contained in the file 40651

simultaneously. Once more, we stress that only the general quality flags are applied in the analysis that follows hereafter.

4 Methodology

The main aim of this study is the assessment of the slice σ_0 noise. In order to pursue this aim, all the "egg" data are binned in 1 dB width bins around five different levels of σ_0, corresponding to low to medium and high wind speed regimes. In practice, for each of the acquisition polarizations, five reference σ_0 levels are computed by averaging the NSCAT4DS Geophysical Model Function (GMF) corresponding to the wind speed values ranging from 5 to 15 ms^{-1} with steps of 2.5 ms^{-1} over the entire spectrum of relative azimuth angles, according to the formula depicted in equation 4.1.

$$\sigma_0^{U_T} \triangleq \frac{1}{2\pi} \int_0^{2\pi} NSCAT4DS(U_T, \phi, \theta, p) d\phi \tag{4.1}$$

where U_T is the desired target wind speed, ϕ is the azimuth angle relative to the antenna, θ is the incidence angle and p is the polarization of the beam (H-Pol or V-Pol). For the sake of completeness, we remind here that the incidence angle of each polarization beam is almost constant, as it is expected for a pencil beam scatterometer such as QuikSCAT. The inner beam (H-Pol) incidence angle is equal to $46.2^o(\pm 0.7^o)$ while the outer beam (V-Pol) one is $54^o(\pm 0.6^o)$. These are the values that have been used in equation 4.1. It is important to remark that the NSCAT4DS GMF has only been used for this purpose and for nothing else.
All the measurements are separated according to:

- the antenna beam polarization
- the view (fore or aft)
- the slice index

As said in section 3, all the $\hat{\sigma}_0$s are QCed by only applying the general quality flags. Then, the operative definition of K_p is applied, which reads as follows:

$$\hat{K}_p \triangleq \frac{\sqrt{E[(\hat{\sigma}_{0i} - \bar{\sigma}_0)^2]}}{\bar{\sigma}_0} \tag{4.2}$$

where the symbol $\hat{}$ stands for "estimation" and $\bar{\sigma}_0$ is the expected value. In this study, this value is set to the so called "egg" value, or, in other words, the computed value for the entire beam footprint (also known as egg), using the slice values. This value is provided in the L1B files. Note that if typically 5 slices were used with equal weight and noise expectation, then equation 4.2 underestimates the noise by about 10%, since the egg $\bar{\sigma}_0$ depends on the slice σ_{0i}. Note that the weight furthermore depends on slice number.

By definition, $\hat{K_p}$ is representative of the noise associated to a set of measurements. It is not possible to associate any $\hat{K_p}$s to any single measurements. Therefore, $\hat{K_p}$ is compared to the median value of K_p ($\tilde{K_p}$) provided in the L1B files. We have chosen the median instead of the average because the K_p distribution is not Gaussian by definition ($K_p > 0$), therefore, the median may be more representative than the average. The median is done over the same dataset. An analysis aiming at assessing the accuracy of both $\hat{K_p}$ and $\tilde{K_p}$ is also proposed.
A sensitivity analysis is then performed, aiming at assessing the presence of any inter slice biases, the presence of any trends of the biases with respect to the acquisition azimuth angle and the presence of any differences between the K_p estimations over the sea and those over all other types of surfaces.
Finally, the random distribution of $\hat{\sigma}_0$s obtained by applying the theoretical model derived from [10] (eq. 2.4) with $\hat{K_p}$ is compared to the distribution obtained with the K_p values provided in the L1B files and to the distribution of the true measurements in the samples.

5 Results and discussion

5.1 Comparison between K_p and $\hat{K}_p$

Figure 2 shows the scatterplot of the K_p values provided in file 40651 versus the corresponding slice $\hat{\sigma}_0$s. Both axis are in logarithmic scale and the dots are colored according to the slice index. The vertical solid (dashed) lines represent the 5 levels of σ_0 used in this study to compare $\hat{K}_p$ with $\tilde{K}_p$ for the H-Pol (V-Pol) acquisitions. As the GMF is a monotonic function of the wind speed, they are ordered from the left to right according to increasing wind speeds. A few things are apparent. First of all, there is a descending trend of K_p until it reaches a plateau, as expected. The asymptotic value of K_p is around 0.3. In addition, it is apparent that, given a value of σ_0, the corresponding K_ps for slice index 0 (K_p^0s) are the largest, while K_p^4s are the lowest. Furthermore, $K_p^{1,7}$s seem to have similar values while K_p^6s seem to rank the second lowest. However, not all colors are visible because some of them are hidden, therefore, this preliminary analysis is not exhaustive, and additional figures will better clarify this aspect. Anyway, these features are sufficiently clear to conclude that, given a σ_0 value, K_p is not symmetric with respect to the slice index, as instead expected. Indeed, the inner slices of the egg are expected to be less noisy than those peripheral.

Figures 3 shows the trend of $\hat{K}_p$ and $\tilde{K}_p$ with respect to the slice index for each of the four flavours *pol-view* and for all the wind speeds analyzed in this study. In particular, the blue markers represent the values obtained on every type of surface (subscript A), while the red markers refer to the sea surface only (subscript S). In order to avoid any ice contamination, the analysis related to the sea surface measurements is limited to the latitude range $\pm 60^o$. The total number of samples are reported in blue and red with the same color code. For the sake of clarity, the y-axis of all the figures have the same range, expressed in percentage ($K_p * 100$). Note that some very high values, such as for example $\tilde{K}_p^0$ at wind speed regimes 5 and 7.5 ms^{-1} (figures 3a and 3b), are not visible.

A few things are apparent from these pictures: a) H-Pol acquisitions are noisier than V-Pol ones. This is particularly true at low wind speed regimes; b) the higher the wind regime is, the higher is the σ_0 and the lower is K_p, as expected, because SNR increases with σ_0; c) $\tilde{K}_p$ is not symmetric with respect to the central slice indices. The symmetry is expected because SNR is higher for the central slices with respect to those peripheral. Indeed, this trend is rather visible for $\hat{K}_p$. In addition, $\tilde{K}_p^{0,1}$ seem to be overestimated with respect to $\hat{K}_p^{0,1}$, while the opposite happens for $\tilde{K}_p^{6,7}$; d) there are no remarkable differences between the fore and aft views; e) finally there are

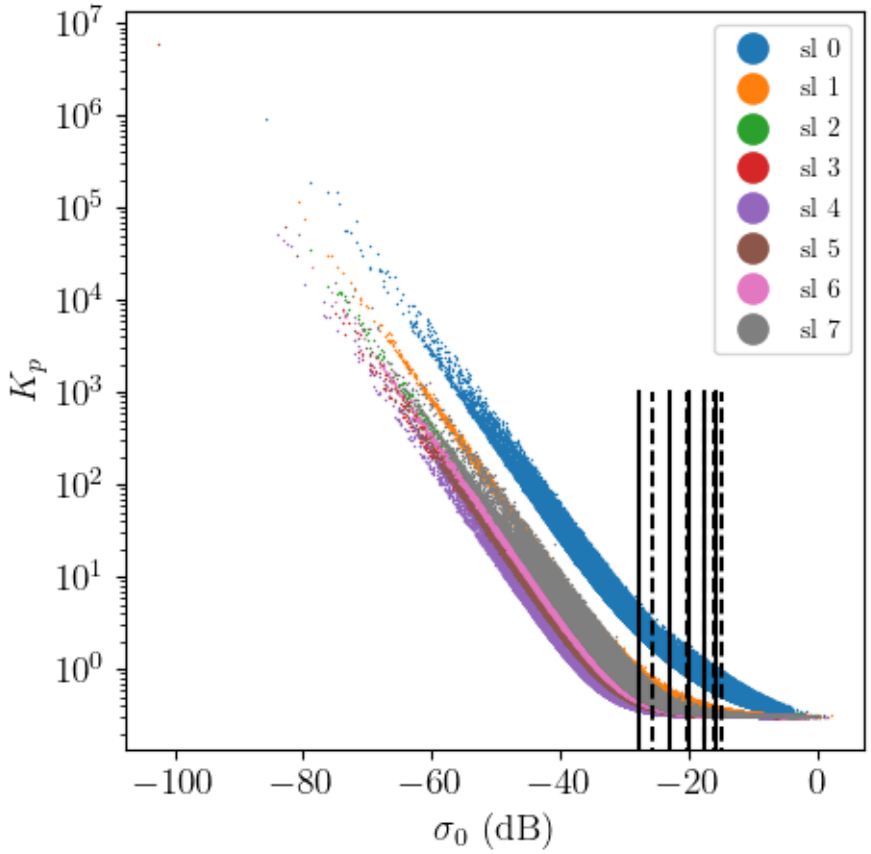

Figure 2: Scatter plot of K_p provided in file 40651 vs slice σ_0. Both axis are in logarithmic scale. Black solid (dashed) vertical lines: σ_0 levels used to compare $\hat{K}_p$ with $\bar{K}_p$ for H-Pol (V-Pol) acquisitions.

almost no differences between $\tilde{K}_{pS}$ and $\tilde{K}_{pA}$, while these are apparent for $\hat{K}_{pS}$ and $\hat{K}_{pA}$. In particular, $\hat{K}_{pS}$ is lower than $\hat{K}_{pA}$, as expected. Indeed, σ_0 is expected to be less variable over sea than over land, ice and mixed surfaces.

Figure 4 reports the values of $\hat{K}_p$ and $\tilde{K}_p$ for the sea acquisitions depicted in figure 3. In order to have an idea of the variability of the K_p values provided in the L1B files, also the standard deviation of each distribution (σ_{K_p}) is reported in parenthesis next to $\tilde{K}_p$. It is apparent that K_p has a wide variability, especially at low wind regimes, for H-Pol acquisitions and for slice index 0.

It is important to stress that both $\sigma_{\tilde{K}_p}$ and $\sigma_{\hat{K}_p}$ are much smaller than σ_{K_p}. In order to assess a measure of the inaccuracies affecting $\tilde{K}_p$ and $\hat{K}_p$, the following analysis has been carried out. The original dataset of sea acquisitions has been randomly sampled n_m times without any repetitions, with $m \in \{3, 10, 30, 100, 300, 1000, 5000\}$, $n_m = \lfloor \frac{N}{m} \rfloor$, N the total amount of available samples and $\lfloor \rfloor$ the symbol for floor division. Then, for each set of m samples, the median of K_p ($\tilde{K}_p^{l_m}$) and $\hat{K}_p^{l_m}$ have been computed, where $l_m \in \{1, \ldots, n_m\}$. Finally, the median of $\{\tilde{K}_p^{l_m}\}$ ($\tilde{\tilde{K}}_p^m$) and $\{\hat{K}_p^{l_m}\}$ ($\tilde{\hat{K}}_p^m$) and the percentiles 2.5 ($pc_{2.5}^m$) and 97.5 ($pc_{97.5}^m$) have been computed. The difference between $pc_{97.5}^m$ and $pc_{2.5}^m$ represents the 95% confidence interval (c.i.) of each distribution, which can be considered a measure of the uncertainty affecting $\tilde{\tilde{K}}_p^m$ and $\tilde{\hat{K}}_p^m$. In the limit of $m \longrightarrow N$, $\tilde{\tilde{K}}_p^m \longrightarrow \tilde{K}_p$ and $\tilde{\hat{K}}_p^m \longrightarrow \hat{K}_p$.

Figure 5 shows the median values as function of m together with the 95% confidence interval for both $\tilde{\hat{K}}_p^m$ (crosses and solid line respectively) and $\tilde{\tilde{K}}_p^m$ (circles and dashed line respectively) distributions. $\hat{K}_p$ and $\tilde{K}_p$ (obtained with the total amount of samples) are depicted with the horizontal dotted and dash-dotted lines respectively. Figure 5a shows the plot for the slice index 0, H-Pol, $U = 5$ ms^{-1}, while figure 5b shows the plot for the slice index 6, V-Pol, $U = 15$ ms^{-1}. The first plot depicts a very noisy case. In addition, $\hat{K}_p$ and $\tilde{K}_p$ are very different. The second one depicts a low-noise case, and $\hat{K}_p$ and $\tilde{K}_p$ tend to the same value. This is in agreement with the values shown in figure 4. As the statistics of both $\hat{K}_p$ and $\tilde{K}_p$ are not affected by the view (aft or fore), the dataset for both views have been merged, in order to have a larger number of samples. The value N reported in the figures 5a and 5b is the sum of the corresponding values reported in the figures 3a (HHA+HHF) and 3e (VVA+VVF) respectively. A few things are apparent from these two figures. a) $\tilde{\hat{K}}_p$ has an asymptotic trend with increasing m. This is to say that the number of samples plays a fundamental role in assessing $\hat{K}_p$. In particular, if $m > 1000$, the asymptotic value is reached. This leads to the conclusion

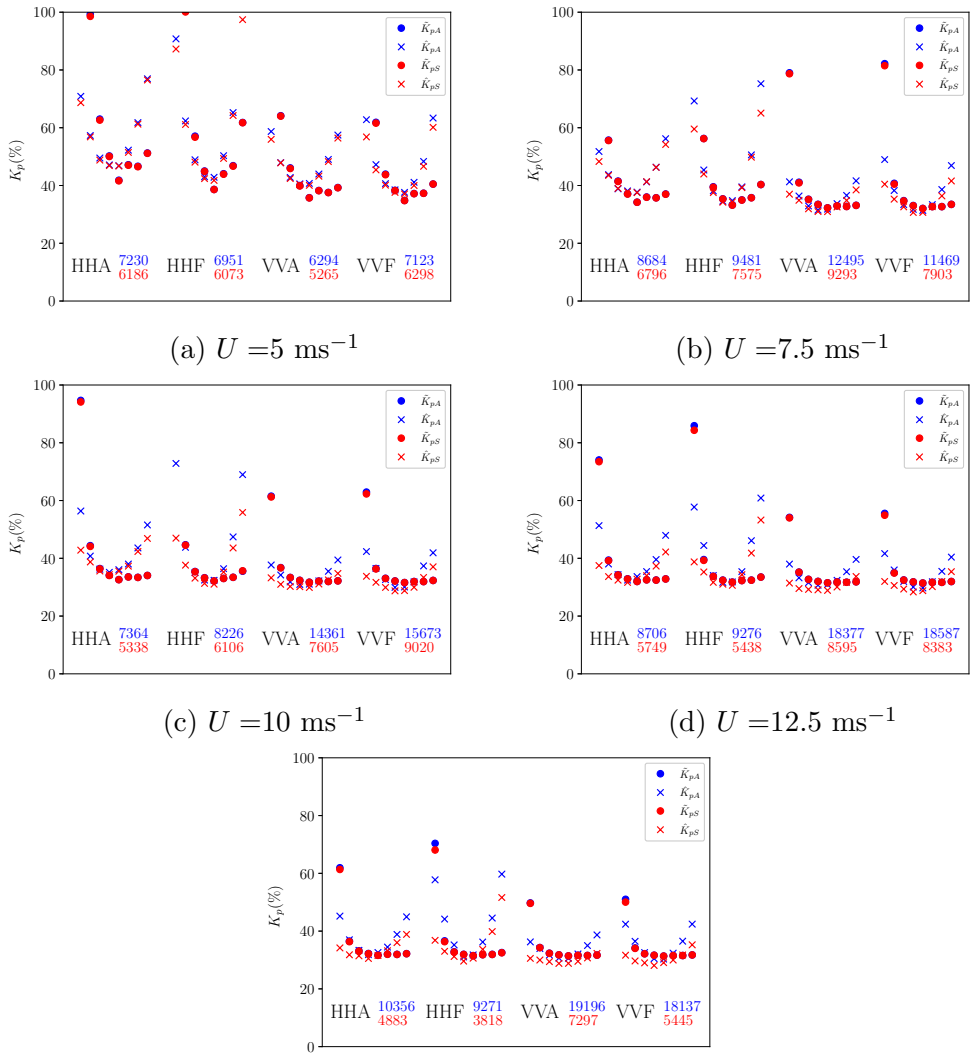

(a) U =5 ms^{-1}

(b) U =7.5 ms^{-1}

(c) U =10 ms^{-1}

(d) U =12.5 ms^{-1}

(e) U =15 ms^{-1}

Figure 3: Blue (red) circles: median of the K_p values (in percentage) provided in file 40651 vs the slice index for every type of surface (marked with subscript A) (sea, marked with subscript S)) and for each of the 4 flavours *pol-view*, namely H-Pol Aft (HHA), H-Pol Fore (HHF), V-Pol Aft (VVA) and V-Pol Fore (VVF). Blue (red) crosses: estimated values of K_p for every type of surface (sea). The number in blue (red) by the flavour label represents the total number of samples for every type of surface (sea). Plots 3a to 3e relate to σ_0 level corresponding to the wind speed indicated in the caption.

	sl 0	sl 1	sl 2	sl 3	sl 4	sl 5	sl 6	sl 7
HHA	68 (281±28308)	56 (98±3175)	48 (62±15953)	46 (50±151)	46 (41±108)	51 (47±932)	61 (46±12071)	76 (51±566)
HHF	87 (363±8916)	61 (100±8518)	48 (56±9395)	42 (44±137)	41 (38±1958)	49 (43±126)	64 (46±674)	97 (61±1035)
VVA	55 (157±874)	47 (64±68)	42 (45±45)	40 (39±35)	40 (35±7)	43 (38±16)	48 (37±48)	56 (39±99)
VVF	56 (160±2783)	45 (61±213)	40 (43±22)	37 (38±5)	37 (34±5)	39 (37±19)	46 (37±27)	60 (40±151)

(a) U =5 ms^{-1}

	sl 0	sl 1	sl 2	sl 3	sl 4	sl 5	sl 6	sl 7
HHA	48 (136±1472)	43 (55±62)	39 (41±356)	37 (37±106)	37 (34±49)	41 (35±21)	46 (35±23)	54 (36±156)
HHF	59 (173±1148)	43 (56±51)	37 (39±39)	34 (35±16)	34 (33±3)	39 (34±66)	49 (35±16)	65 (40±9591)
VVA	36 (78±19)	34 (40±5)	31 (35±2)	30 (33±1)	30 (32±0)	32 (32±1)	34 (32±1)	38 (33±1)
VVF	40 (81±27)	35 (40±41)	32 (34±2)	30 (32±0)	30 (32±0)	32 (32±1)	36 (32±1)	41 (33±5)

(b) U =7.5 ms^{-1}

	sl 0	sl 1	sl 2	sl 3	sl 4	sl 5	sl 6	sl 7
HHA	42 (94±408)	38 (44±107)	35 (36±12)	34 (34±10)	35 (32±7)	37 (33±7)	42 (33±10)	46 (34±40)
HHF	46 (114±176)	37 (44±17)	33 (35±20)	31 (33±1)	31 (32±0)	35 (33±1)	43 (33±19)	55 (35±36)
VVA	33 (61±10)	30 (36±2)	30 (33±0)	30 (32±0)	29 (31±0)	31 (32±0)	32 (31±0)	34 (32±0)
VVF	33 (62±13)	31 (36±2)	29 (33±0)	28 (32±0)	28 (31±0)	29 (31±0)	33 (31±0)	37 (32±0)

(c) U =10 ms^{-1}

	sl 0	sl 1	sl 2	sl 3	sl 4	sl 5	sl 6	sl 7
HHA	37 (73±86)	33 (39±6)	32 (34±1)	31 (32±1)	32 (31±0)	33 (32±1)	37 (32±3)	42 (32±6)
HHF	38 (84±11860)	35 (39±19)	31 (33±1)	31 (32±0)	30 (31±0)	34 (32±0)	41 (32±12)	53 (33±9)
VVA	31 (53±7)	29 (35±1)	29 (32±0)	29 (31±0)	28 (31±0)	30 (31±0)	31 (31±0)	33 (31±0)
VVF	31 (54±7)	30 (34±1)	29 (32±0)	28 (31±0)	28 (31±0)	30 (31±0)	31 (31±0)	35 (31±0)

(d) U =12.5 ms^{-1}

	sl 0	sl 1	sl 2	sl 3	sl 4	sl 5	sl 6	sl 7
HHA	34 (61±13)	31 (36±2)	31 (33±2)	30 (32±0)	31 (31±0)	33 (31±0)	36 (31±0)	38 (32±2)
HHF	36 (68±96)	33 (36±3)	31 (32±0)	29 (31±0)	30 (31±0)	33 (31±0)	39 (31±0)	51 (32±4)
VVA	30 (49±5)	29 (34±1)	29 (32±0)	28 (31±0)	28 (31±0)	29 (31±0)	30 (31±0)	32 (31±0)
VVF	31 (50±6)	29 (34±1)	29 (32±0)	28 (31±0)	29 (31±0)	29 (31±0)	31 (31±0)	35 (31±0)

(e) U =15 ms^{-1}

Figure 4: $\hat{K_p}$ ($\tilde{K_p} \pm \sigma_{K_p}$) for sea measurements, for the four *pol-view* flavours and for each slice. a) to e) refer to the different wind regimes considered in this study.

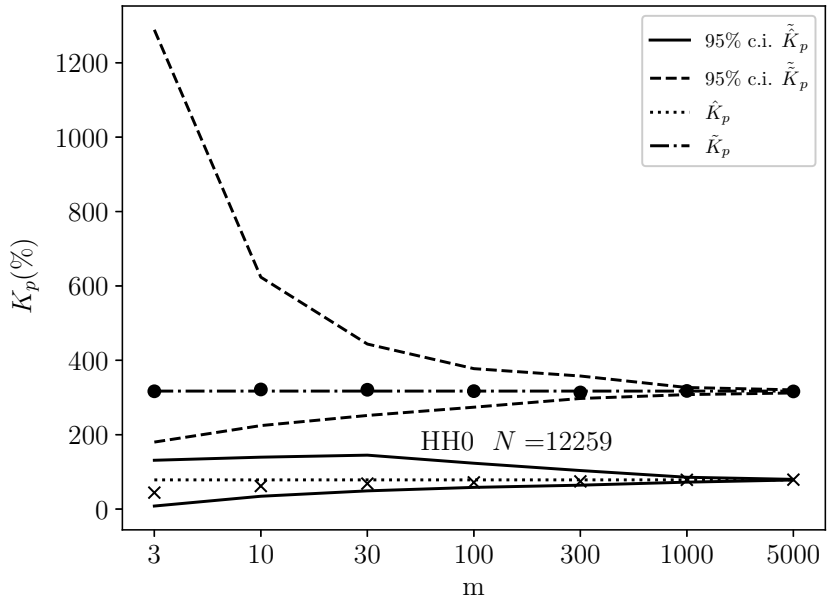

(a) Slice index equal to 0, H-Pol, U =5 ms^{-1}

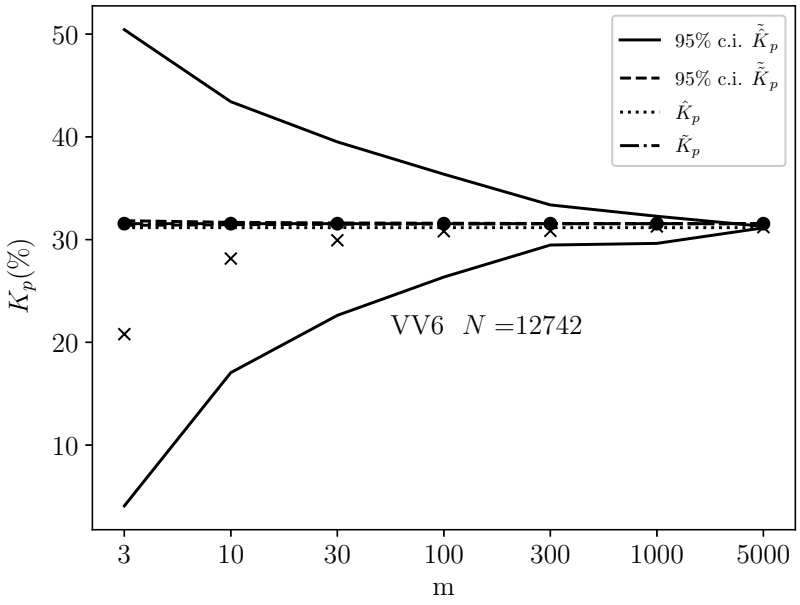

(b) Slice index equal to 6, V-Pol, U =15 ms^{-1}

Figure 5: Solid (dashed) lines: 95% confidence interval for the median of the estimated (provided) K_p obtained with m samples. Crosses (circles): median of the estimated (provided) K_p obtained with m samples. Dotted (line dotted) line: $\hat{K}_p$ estimated (median of the K_p values provided) with the total available N samples in file 40651.

that the number of samples we use for estimating $\hat{K}_p$ is adequate. This is not the case of $\tilde{\tilde{K}}_p$, which are rather constant; b) in addition, both $\hat{\tilde{K}}_p$ and $\tilde{\tilde{K}}_p$ distributions are not symmetric w.r.t. their median value. This is expected because, as said before, K_p is positive-definite; c) the $\tilde{\tilde{K}}_p$ distribution is rather wide in the first case, especially for $m < 100$, confirming that this is a very noisy case; d) finally, and most important, the two distributions are well separated in the first case. This is to say that $\tilde{K}_p$ is effectively overestimated w.r.t. $\hat{K}_p$, as predicted before. In the second case, the 95% confidence interval of $\tilde{\tilde{K}}_p$ is almost not distinguishable from the line of $\tilde{K}_p$, confirming that the noise is very low.

5.2 Inter-slice biases

The upper plot of figure 6a (6b) shows the normalized density scatter plot of the H-Pol (V-Pol) slice σ_0s with index 7 (σ_0^7) versus σ_0^0. The statistics relating to the relative bias, standard deviation, correlation index, and the total number of samples (N) are reported on the plot. The density is normalized to its maximum value. The red solid (dashed) line of the bottom plot of figure 6a (6b) shows the relative bias of σ_0^7 vs σ_0^0 (σ_0^0 vs σ_0^7), while the blue lines depict the standard deviation of the differences. Their y-axis is reported on the right of the plot. Solid and dashed have the same code of the red lines.
Figure 6 shows once more that the H-Pol measurements are noisier than those V-Pol, in agreement with the previous conclusions. The relative bias is not well visible, since the scatter plots appear rather symmetric w.r.t. the diagonal. However, the red curves of the bottom plots, do not overlap, showing that σ_0^0 is generally smaller than σ_0^7. The relative standard deviation curves (blue curves) do not show any meaningful differences between the statistics of σ_0^0 vs σ_0^7 and σ_0^7 vs σ_0^0, but for high values of σ_0. However, these may be due to poor sampling.

Figure 7a (7b) integrates the inter-slice σ_0 biases in dB. The plot is symmetric w.r.t. the main diagonal of the matrix. The color bars of the figures 7a and 7b are identical in order to make the comparison easier. Both figures should be read as lower triangular matrices (or upper triangular) since the two triangular parts are anti-symmetric. It is rather evident that there are some inter slice biases and that they are more relevant for H-Pol acquisitions than for those V-Pol. The inter slice bias may reach 0.8 (0.3) dB for the H-Pol (V-Pol) acquisitions, and it increases with the relative distance between the slices.

Figure 8a (8b) shows the dependency of the H-Pol (V-Pol) slice σ_0 biases

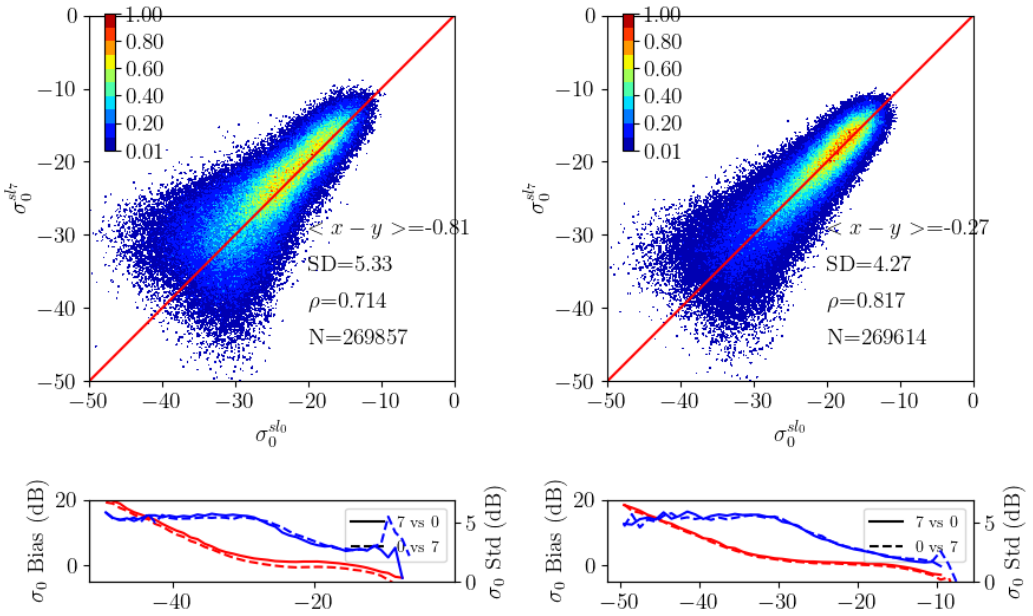

(a) H-Pol (b) V-Pol

Figure 6: Upper left (right) plot: scatter plot of H-Pol (V-Pol) slice σ_0 with index 7 (σ_0^7) vs slice σ_0 with index 0 (σ_0^0). The bias, standard deviation, correlation coefficient and number of samples are reported in the plot. The normalized density (the maximum density of samples is equal to 1) of the samples is colored according the color bar in the upper left corner. Bottom left (right) plot: relative bias of H-Pol (V-Pol) σ_0^7 vs σ_0^0 (σ_0^0 vs σ_0^7) as function of σ_0 depicted with the red solid (dashed) line. The blue lines depict the standard deviation of the differences. Dashed and solid lines have the same meanings of the blue lines. Their y-axis is reported on the right of the plot

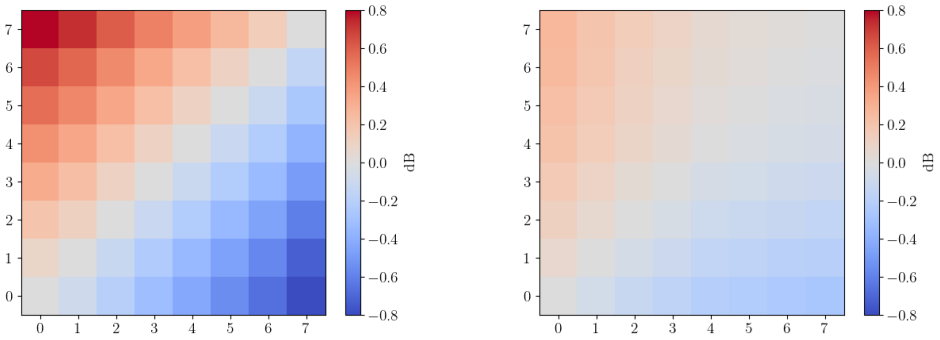

(a) H-Pol (b) V-Pol

Figure 7: Inter-slice σ_0 biases in dB.

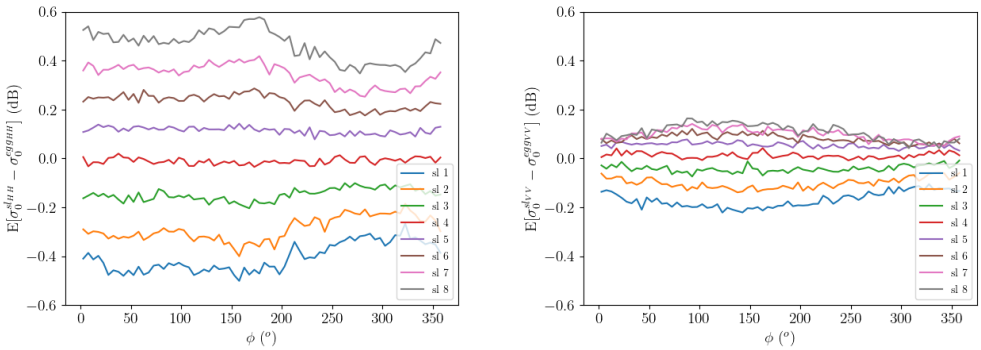

(a) H-Pol (b) V-Pol

Figure 8: Dependency of the slice σ_0 bias w.r.t. the acquisition azimuth angle. Data refer to the entire day 10^{th} of April 2007.

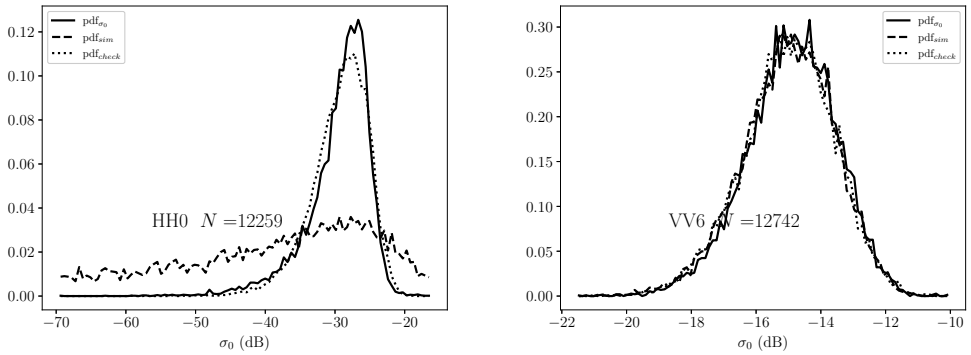

(a) slice index 0, H-Pol, U =5 ms^1 (b) slice index 6, V-Pol, U =15 ms^1

Figure 9: Solid line: distribution of the σ_0 measurements $\hat{\sigma}_0$. Dashed (dotted) line: distribution of the simulated σ_0 obtained with the model described in 2.4, using the K_p provided in the L1B file ($\hat{K}_p$). The total number of samples is reported in the plot.

computed w.r.t. the σ_0^{egg} as function of the acquisition azimuth angle (ϕ). The axes are the same for both panels, in order to make the comparison easier. Once more, it is apparent that H-Pol σ_0s are more biased than the V-Pol ones. This may be related to the incidence angle change from slice 0 to 7, which is systematic and about 2 degrees over the full slice range. The H-Pol GMF suggests a decrease of about 1 dB from slice 0 to 7, somewhat depending on wind speed and wind direction. For V-Pol, the dependencies are similar, but the mean change is only about 0.5 dB. The effect may be more accurately simulated by using the ECMWF winds and GMF for each slice sample to replace the measured backscatter values. However, since the effect as a function of incidence angle is quasi-linear at any given speed and direction, an egg incidence angle, weighted in the same way as the backscatter values, will provide accurate wind retrievals. In addition, there is a clear trend of the H-Pol σ_0 biases for $\phi > 200^o$. A small trend is also observed for V-Pol acquisitions. These small variations may be due to the changes in wind speed and direction sample for each bin. Note, for example, that the wind direction PDF as globally sampled by a scatterometer varies by a factor of 2 [11]. Different beam azimuth pointing directions in fact shift this distribution over the upwind, crosswind and downwind directions.

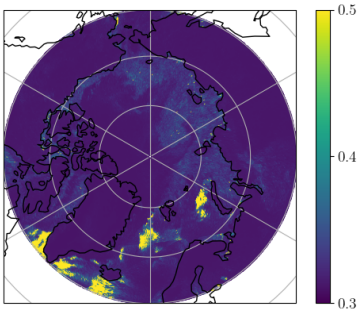

(a)

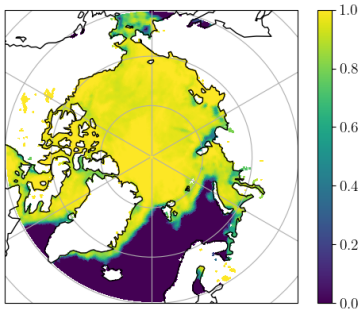

(b)

Figure 10: Left plot: K_p for slice index 3, V-Pol, fore over the North Pole on the 10^{th} of April 2007. Right plot: Ice cover from ECMWF ERA5 reanalysis on the same day at 18:00 UTC.

5.3 Validation of the $\hat{\sigma_0}$ distribution model

The solid line of figure 9a (9b) shows the σ_0 distribution for the slice index 0 (6), H-Pol (V-Pol) and U =5 ms^{-1} (U =15 ms^{-1}) (the same cases shown in figure 5). The dashed (dotted) line represents the distribution of the simulated σ_0s obtained with the model described in equation 2.4 by using the values of K_p provided in the L1B file ($\hat{K}_p$). Figure 9b shows that the distributions of the simulated σ_0s well overlap with the true distribution, regardless of the value of K_p used in the model. In this case, $\hat{K}_p$ and $\tilde{K}_p$ are almost identical. This result demonstrates the goodness of the distribution model. Instead, figure 9a shows that the distribution of the σ_0s simulated with $\hat{K}_p$ is very close to the true distribution, confirming the robustness of the estimation methodology of K_p applied in this study. On the other side, the distribution obtained with the K_ps provided in the L1B files is much wider than the measured one, showing, once more, that K_ps are generally overestimated in this case.

5.4 K_p and sea-ice coverage

Taking inspiration from [12], a quick visual analysis about the presence of any correlations between K_p and ice cover over the Nort Pole is proposed. Figure 10a shows the values of K_p from the L1B files for the slice index 3, V-Pol, fore (K_p^{VVF3}) over the North Pole on the 10^{th} of April 2007, while figure 10b shows the corresponding ice cover from ECMWF ERA5 reanalysis [13] at 18:00 UTC (i.e., 18-hour forecast from 00 UTC analysis time). It is

apparent that there is a visual correlation between K_p and the borders of the ice cap. In practice it seems that close to the borders of the ice cap, K_p increases, certifying the presence of a larger variability in the σ_0 in those areas. Such aspect deserves a thorough investigation, which is beyond the scope of this study. Similar effects occur near the land-sea boundaries and will be handled in a coastal processing in future work.

6 Conclusions

In this work, an accurate assessment of the QuikSCAT slice σ_0 noise is carried out.
The methodology used, which is based on the common definition of K_p, is described as implemented and applied in order to estimate a unique value of K_p ($\hat{K}_p$) for the QuikSCAT slice σ_0 measurements. This value, based on an entire orbit, is compared to the median value of the K_ps ($\tilde{K}_p$) provided in the L1B files with each measurement and which are estimated from relevant instrument parameters.
Some sensitivity analysis is carried out in order to verify the dependency on the wind regime, the type of surface (sea or any other type), the slice position w.r.t. the egg centroid (slice index) and on the view (aft or fore), as well as the presence of any slice biases and their dependency on the acquisition azimuth angle. In addition, a theoretical σ_0 distribution model has been implemented and validated against the real measurements. Finally, a visual analysis on the correlation between K_p and the ice edge is provided over the North Pole.
Both $\hat{K}_p$ and $\tilde{K}_p$ have a decreasing trend with increasing wind speed. This is in line with expectations, since the higher the wind speed is, the higher is the SNR and the lower is K_p. Due to the lower signal, H-Pol acquisitions are generally noisier than V-Pol ones, while for the same backscatter value, the noise properties are very similar. No appreciable differences are present when discriminating between the scatterometer views (aft or fore), while the type of surface plays a non-negligible role. However, while $\hat{K}_p$ over sea is generally lower than K_p over every other type of surface, this difference is not appreciable for $\tilde{K}_p$.
Given a σ_0 level, $\hat{K}_p$ has a well defined parabolic trend w.r.t. the slice index. This trend is also expected because the central slices of the egg have a better SNR. However, the trend of $\tilde{K}_p$ is rather different, showing remarkable overestimates for slice indices 0 and 1 and underestimates for slice indices 6 and 7 at all wind speed regimes, when compared to $\hat{K}_p$.
The σ_0 measurements with a given slice index are biased w.r.t. the σ_0^{egg} and these biases have small trends w.r.t. the acquisition azimuth angle. In addition, they are also biased w.r.t. each other, with backscatter values decreasing with the incidence angle. These biases may reach 0.8 dB for H-Pol measurements and 0.3 dB for V-Pol ones, in line with the general GMF sensitivity as a function of incidence angle. Since this sensitivity is quasi-linear at any wind speed or direction, it suggests that slice incidence angles should be weighted in the same way as the contributing backscatter values in each view.

The σ_0 theoretical distribution model proves to be reliable when compared to the distribution of the real measurements. In this study, this tool has been used to further validate the goodness of $\hat{K}_p$, but it can also be used for simulation studies.
Finally, it seems that K_p is larger near the ice edge. This may be explained by the radar cross section contrast between water and ice, resulting in a larger variability in mixed scenes. Hence, besides using the results of this study for dealing with land and sea backscatter segregation in coastal regions, they may also be used for improved water and ice discrimination in future work.

7 Future work

In order to improve the sampling and the accuracy of the QuikSCAT-derived coastal wind field, the following stages are advised and left for the future: a) assess the most effective regression procedure on the slice σ_0s to obtain the sea backscatter value (at LCR=0), before applying the retrieval procedure. In particular, a comparison between the K_p-weighting and the simpler constant weighting will be carried out, both in open-ocean and coastal areas [14] [15]; b) validate the LCR based σ_0 correction scheme [4] in coastal areas; c) implement the retrieval procedure; d) implement the QuikSCAT coastal processor; e) extend the LCR based methodology to other pencil-beam scatterometers.

References

[1] J. Vogelzang, A. Stoffelen, R. D. Lindsley, A. Verhoef, and J. Verspeek, "The ascat 6.25-km wind product," *IEEE Journal of Selected Topics in Applied Earth Observations and Remote Sensing*, vol. 10, pp. 2321–2331, May 2017.

[2] M. P. Owen and D. G. Long, "Land-contamination compensation for quikscat near-coastal wind retrieval," *IEEE Transactions on Geoscience and Remote Sensing*, vol. 47, no. 3, pp. 839–850, 2009.

[3] R. D. Lindsley, C. Anderson, J. Figa-Saldaña, and D. G. Long, "A parameterized ascat measurement spatial response function," *IEEE Transactions on Geoscience and Remote Sensing*, vol. 54, no. 8, pp. 4570–4579, 2016.

[4] J. Vogelzang and A. Stoffelen, "Ascat land correction, report for the eumetsat ocean and sea ice saf," tech. rep., Koninklijk Nederlands Meteorologisch Instituut, 2020. SAF/OSI/CDOP3/KNMI/TEC/TN/384.

[5] G. Grieco, M. Portabella, J. Vogelzang, V. A., and S. A., "Initial development of pencil-beam scatterometer coastal processing," tech. rep., Barcelona Expert Center (BEC ICM-CSIC), 2020. OSI-SAF VS Technical Report # OSI-SAF 20-01.

[6] M. W. Spencer, C. Wu, and D. G. Long, "Improved resolution backscatter measurements with the seawinds pencil-beam scatterometer," *IEEE Transactions on Geoscience and Remote Sensing*, vol. 38, no. 1, pp. 89–104, 2000.

[7] A. Tarantola, *Inverse Problem Theory and Methods for Model Parameter Estimation*. Society for Industrial and Applied Mathematics, 2005.

[8] "https://podaac-opendap.jpl.nasa.gov/opendap/."

[9] Thorlabs, *QuikSCAT Science Data Product. User's Manual*. JPL NASA.

[10] R. E. Fischer, "Standard deviation of scatterometer measurements from space," *IEEE Transactions on Geoscience Electronics*, vol. 10, no. 2, pp. 106–113, 1972.

[11] A. Stoffelen, "A simple method for calibration of a scatterometer over the ocean," *Journal of Atmospheric and Oceanic Technology*, vol. 16, no. 2, pp. 275 – 282, 1999.

[12] C. Anderson, H. Bonekamp, C. Duff, J. Figa-Saldana, and J. J. W. Wilson, "Analysis of ascat ocean backscatter measurement noise," *IEEE Transactions on Geoscience and Remote Sensing*, vol. 50, no. 7, pp. 2449–2457, 2012.

[13] H. Hersbach, B. Bell, P. Berrisford, S. Hirahara, A. Horányi, J. Muñoz-Sabater, J. Nicolas, C. Peubey, R. Radu, D. Schepers, A. Simmons, C. Soci, S. Abdalla, X. Abellan, G. Balsamo, P. Bechtold, G. Biavati, J. Bidlot, M. Bonavita, G. De Chiara, P. Dahlgren, D. Dee, M. Diamantakis, R. Dragani, J. Flemming, R. Forbes, M. Fuentes, A. Geer, L. Haimberger, S. Healy, R. J. Hogan, E. Hólm, M. Janisková, S. Keeley, P. Laloyaux, P. Lopez, C. Lupu, G. Radnoti, P. de Rosnay, I. Rozum, F. Vamborg, S. Villaume, and J.-N. Thépaut, "The era5 global reanalysis," *Quarterly Journal of the Royal Meteorological Society*, vol. 146, no. 730, pp. 1999–2049, 2020.

[14] M. Portabella and A. Stoffelen, "Characterization of residual information for seawinds quality control," *IEEE Transactions on Geoscience and Remote Sensing*, vol. 40, no. 12, pp. 2747–2759, 2002.

[15] A. Stoffelen and M. Portabella, "On bayesian scatterometer wind inversion," *IEEE Transactions on Geoscience and Remote Sensing*, vol. 44, no. 6, pp. 1523–1533, 2006.